

Optimized Radiofrequency Coil Setup for MR Examination of Living Isolated Rat Hearts in a Horizontal 9.4T Magnet

Maelene Lohezic,^{1†} Christian Bollensdorff,^{2,3†} Matthias Korn,⁴ Titus Lanz,⁴ Vicente Grau,⁵ Peter Kohl,^{2,6} and Jürgen E. Schneider^{1*}

Purpose: (i) To optimize an MR-compatible organ perfusion setup for the nondestructive investigation of isolated rat hearts by placing the radiofrequency (RF) coil inside the perfusion chamber; (ii) to characterize the benefit of this system for diffusion tensor imaging and proton (¹H-) MR spectroscopy.

Methods: Coil quality assessment was conducted both on the bench, and in the magnet. The benefit of the new RF-coil was quantified by measuring signal-to-noise ratio (SNR), accuracy, and precision of diffusion tensor imaging/error in metabolite amplitude estimation, and compared to an RF-coil placed externally to the perfusion chamber.

Results: The new design provided a 59% gain in signal-to-noise ratio on a fixed rat heart compared to using an external resonator, which found reflection in an improvement of living heart data quality, compared to previous external resonator studies. This resulted in 14–29% improvement in accuracy and precision of diffusion tensor imaging. The Cramer–Rao lower bounds for metabolite amplitude estimations were up to 5-fold smaller.

Conclusion: Optimization of MR-compatible perfusion equipment advances the study of rat hearts with improved signal-to-noise ratio performance, and thus improved accuracy/precision. *Magn Reson Med* 73:2398–2405, 2015. © 2014 The Authors. Magnetic Resonance in Medicine Published by

Wiley Periodicals, Inc. on behalf of International Society of Medicine in Resonance. This is an open access article under the terms of the Creative Commons Attribution License, which permits use, distribution, and reproduction in any medium, provided the original work is properly cited.

Key words: cardiac magnetic resonance imaging; radiofrequency coil; Langendorff perfusion; diffusion tensor imaging; proton spectroscopy

INTRODUCTION

Langendorff-perfused hearts are a well-established and important model in fundamental cardiac research, as this technique provides well-controlled conditions for manipulation and observation of the living heart (1). For MR imaging and spectroscopy (MRS), the Langendorff-perfused heart represents an important intermediate model system between in vivo beating hearts and ex vivo fixed organ preparations, as it provides good control over cardiac motion (hearts can be arrested, paced, or allowed to beat freely), eliminates respiratory motion, and avoids the need for localized MRS experiments (2). This model system has been used extensively to study cardiac metabolism with ¹H- (3,4) and ³¹P-MRS (5,6), but also ²³Na- (7), ¹³C- (8), and ³⁹K/⁸⁷Rb-MRS (9,10). Moreover, it has been widely used for the development and validation of new cardiac MRI techniques such as first-pass cardiac perfusion (11), flow measurements (12), myocardial arterial spin labeling (13), or diffusion tensor imaging (DTI) (14–18), where the bulk motion of the heart represents a major challenge. In vivo cardiac DTI, for instance, requires (i) careful synchronization with the cardiac mechanical activity and (ii) appropriate acquisition strategies to handle respiratory motion. For the latter, either free-breathing approaches, with respiratory gating (19), or breath hold, that is facilitated by acceleration techniques (20), have been utilized. The use of strong gradient systems (21) and motion-compensated approaches (22) further reduces DTI sensitivity to motion. Consequently, its application in small animals has only been demonstrated very recently (23), and clinically relevant applications are emerging (24–26).

Isolated heart experiments are typically conducted on MR systems with vertical bore magnets, as perfusing hearts in a horizontal magnet give rise to additional technical challenges in terms of solution handling. Recently,

¹Division of Cardiovascular Medicine, Radcliffe Department of Medicine, University of Oxford, Oxford, UK.

²National Heart and Lung Institute, Imperial College London, London, UK.

³Qatar Cardiovascular Research Center, Qatar Foundation, Doha, Qatar.

⁴Rapid Biomedical GmbH, Rimpf, Germany.

⁵Department of Engineering Science, University of Oxford, Oxford, UK.

⁶Department of Computer Science, University of Oxford, Oxford, UK.

Grant sponsor: BBSRC Grant; Grant number: BB/I012117/1; Grant sponsor: British Heart Foundation (BHF) Centre for Research Excellence; Grant sponsor: BHF Senior Basic Science Research Fellowship (to J.E.S. and P.K.); Grant numbers: FS/11/50/29038 and FS/12/17/29532; Grant sponsor: BHF New Horizon Grant (to V.G. and P.K.); Grant number: NH/13/30238; Grant sponsor: Wellcome Trust Core Award; Grant number: 090532/Z/09/Z.

*Correspondence to: Jürgen E. Schneider, Ph.D., BMRU, Wellcome Trust Center for Human Genetics, Roosevelt Drive, Oxford OX3 7BN, UK. E-mail: jurgen.schneider@cardiov.ox.ac.uk

[†]These authors contributed equally to this work.

Correction added after online publication 5 August 2014. The statement of equal contribution of authorship moved from the acknowledgments to the authors' footnote.

The copyright line for this article was changed on 29 September 2014 after original online publication.

Received 18 April 2014; revised 12 June 2014; accepted 24 June 2014

DOI 10.1002/mrm.25369

Published online 12 July 2014 in Wiley Online Library (wileyonlinelibrary.com). © 2014 The Authors. Magnetic Resonance in Medicine Published by Wiley Periodicals, Inc. on behalf of International Society of Medicine in Resonance. This is an open access article under the terms of the Creative Commons Attribution License, which permits use, distribution, and reproduction in any medium, provided the original work is properly cited.

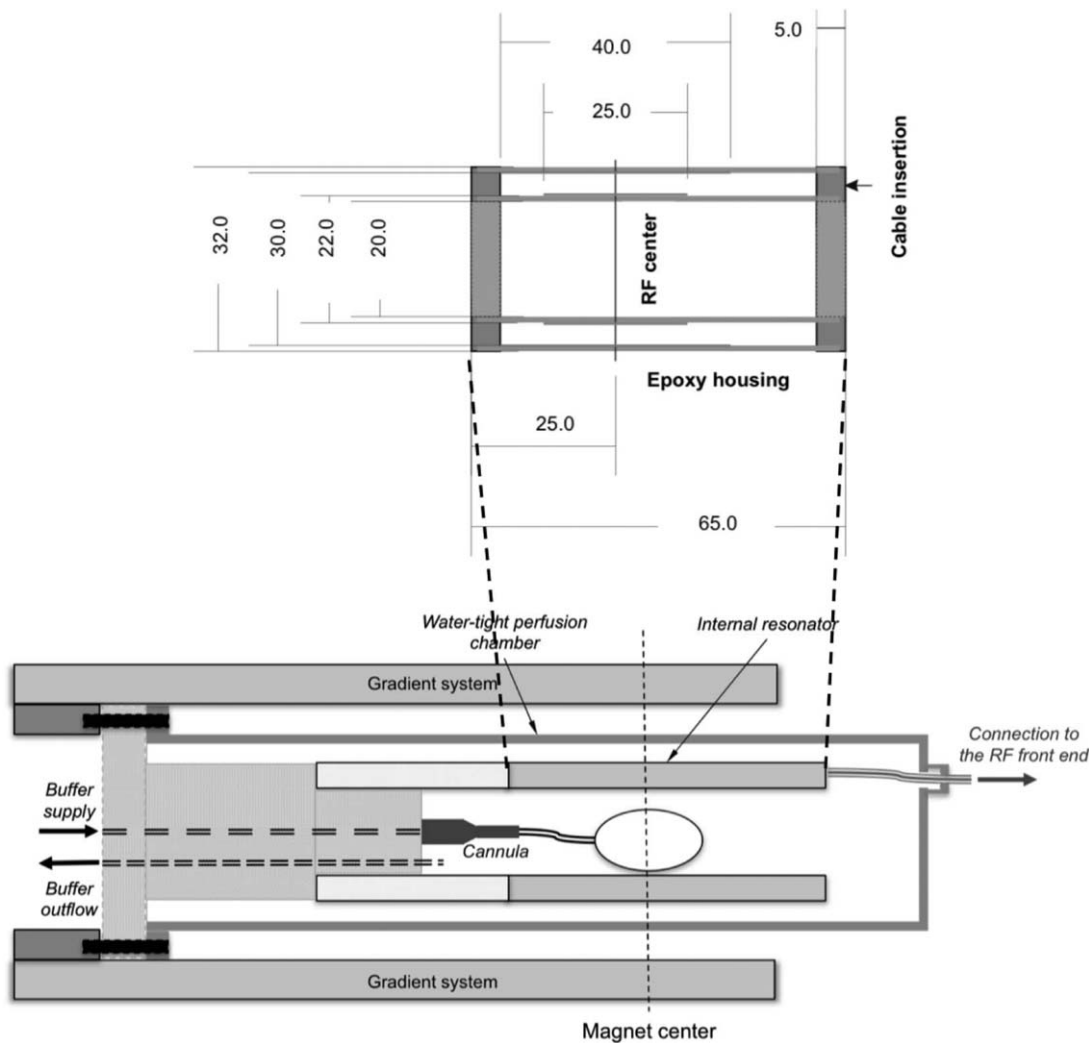


FIG. 1. Optimized setup for MR examination of living, Langendorff-perfused rat hearts. Top: Schematics of the dimensions (in mm) of the internal birdcage resonator. Bottom: Integration of the transmit/receive resonator in the perfusion chamber.

Hales et al. developed a custom-made perfusion rig for use in a horizontal magnet to noninvasively assess myocardial fiber architecture in two different mechanical states (slack and contracture) in one and the same living heart (18). In particular, they demonstrated that not only the modification of the fiber helical structure, but also an accordion-like rearrangement of transmural sheet population alignment contribute to ventricular wall deformation during cardiac contraction. In their design, the MR setup was completely decoupled from the perfusion rig, using a radiofrequency (RF) coil outside the sealed chamber containing the heart. This resulted in limited MR sensitivity, thus requiring multiple averages and long scan times to achieve adequate spatial resolution and signal-to-noise ratio (SNR).

Refinement of RF-coil technology is an obvious way to improve SNR of MR experiments, for example, to enhance the performance of DTI measurements (27). Here, we report a novel design that uniquely integrates the RF-coil into the organ perfusion chamber (i.e., a corrosive environment), to increase the filling factor, and, therefore, SNR. A comprehensive set of experiments was conducted

to quantify the benefit of this new RF-coil design by assessing SNR, accuracy and precision of DTI experiments and SNR/accuracy of amplitude estimates in ^1H -MRS.

METHODS

Hardware

MR System

All experiments were performed using a 9.4T (400 MHz) MR system (Agilent Technologies, Santa Clara, CA), comprising a horizontal magnet (bore size 210 mm), a VNMRS Direct Drive console, and a shielded gradient system (1 T m^{-1} , rise time $130\text{ }\mu\text{s}$, inner diameter 60 mm).

RF-Coil Design

A quadrature driven birdcage resonator (28) was designed and used for transmission (Tx) and reception (Rx) of the NMR signal (Fig. 1—top). To increase the filling factor of the previous setup, and thus improve the SNR, the resonator (diameter: 22 mm, length: 25 mm) was integrated inside the perfusion chamber

Table 1
Acquisition Parameters

Experiments	Pulse sequence	Acquisition parameters
B ₁ efficiency	Nonselective excitation pulse followed by 3 × 180° slice selective pulses	TE/TR = 27/1000 ms; FOV = 22 × 22 mm (128 × 128); volume selected = (4 mm) ³
B ₁ map	Slice selective two-dimensional spin echo, 10π non-localized preparation pulse followed by gradient spoiler (pulse length for 2π pulse as determined above)	TE/TR = 11/1000 ms; FOV = 22 × 22 mm (256 × 256); slice thickness = 1 mm
SNR map	Slice selective two-dimensional gradient echo	TE/TR = 3/100 ms; flip angle = 20°; FOV = 20 × 20 mm (128 × 128); slice thickness = 1 mm
DTI	Two-dimensional multislice fast spin echo with diffusion sensitizing unipolar gradients	TE _{eff} /TR = 15/1000 ms; 8 echoes; FOV = 20 × 20 mm (128 × 128); slice thickness = 1 mm; 13 slices; 12 averages G = 31 G cm ⁻¹ ; δ = 2.5 ms; Δ = 9.6 ms; b _{max} = 508 s mm ⁻²
¹ H MRS	Point resolved spectroscopy (PRESS)	TE/TR = 135/15000 ms; bandwidth = 4 kHz; no water suppression: 8, 32, 64 averages; water suppressed: 256 averages; volume selected = (4 mm) ³
Perfused heart MRI	Two-dimensional multislice spin echo	TE/TR = 5/2500 ms; FOV = 20 × 20 mm (128 × 128); slice thickness = 1 mm; 2 averages

TE: echo time; TE_{eff}: effective TE; TR: repetition time; FOV: field of view; G: diffusion gradient strength; δ: gradient duration; Δ: gradient separation; b_{max}: maximum *b* value (including imaging gradients and cross-terms between imaging and diffusion gradients).

(Fig. 1—bottom). The wall thickness of the housing between the internal birdcage resonator and isolated organ was 1 mm, resulting in an inner diameter of 20 mm for the resonator housing, suitable for the size of isolated rat hearts (typical diameter 14–16 mm, length 18–22 mm). Flexible circuit material (8 μm copper-coated flexible FR4 substrate) was used as RF-shielding. The birdcage resonator was built as a 12-leg high-pass birdcage and fixed tuned-and-matched to 50 Ω at the working frequency of 400 MHz. Cable traps to ensure an electrically symmetric coupling scheme were included within the primary housing of the birdcage resonator. A quadrature hybrid was used for connecting the two resonator channels to the Tx and Rx lines of the MR system. A feature of this design is that the birdcage resonator is placed in the perfusion solution. To protect electronics from ionic fluids and erosion, the housing of the resonator was sealed. The housing itself was made from glass fiber reinforced epoxy and the end-plates of PMMA and PVC. As moving parts like trimmers are extremely difficult to seal, especially when taking into account restrictions given by the MRI environment and the required reliability and robustness, both channels of the birdcage resonator were fixed tuned-and-matched. This approach was deemed appropriate due to the well-defined load of the isolated rat heart within the perfusion solution.

Experimental Design for Coil Characterization

Quality assessment of the new birdcage resonator included comprehensive coil characterization on the bench and in the magnet. The performance achieved by this coil design (in the following referred to as “internal resonator”) was compared with the tune- and match-able external birdcage resonator (external resonator) used previously (18), i.e., a quadrature driven birdcage Tx/Rx resonator (Rapid Biomedical, Rimpf, Germany) with a mean resonator diameter of 41 mm (housing inner diameter 39 mm) and a length of 39 mm. This coil was tuned

and matched for each loading condition. Bench characterization and imaging validation were conducted on a homogeneous phantom (referred to as “saline phantom”), which was filled with 3-mL saline (170 mM NaCl) to mimic the loading by the perfused rat heart during the subsequent experiments. For MRS validation, another 3-mL phantom (metabolite phantom) was used containing 170 mM NaCl, 10 mM Na-lactate, 10 mM taurine, and 10 mM creatine. Finally, a fixed rat heart (29) was used for comparative MR measurements, to guarantee a stable and comparable biological sample for one-to-one coil comparison.

Bench Measurements

Loaded and unloaded quality factors (*Q*) were determined on a network analyzer (Agilent E5061A, Agilent Technologies, Santa Clara, CA). The reflection coefficient (*S*₁₁) and the channel isolation (*S*₁₂) were also assessed. To simulate loading conditions, the saline phantom was placed in each resonator. *Q* were measured with no coupling network hooked up to the resonator as retuning and rematching was not possible for different loading conditions. This is ameliorated by the fact that the coupling network had no influence on the *Q* value. Tune-and-match settings of the external birdcage resonator were adjusted between measurements.

RF Excitation (B₁) Field

To quantitatively compare the performance of the internal and external resonator in the MR system, the B₁ efficiency was derived from a volume-selective measurement of the 360° flip angle duration at a given Tx power on the saline phantom, and on the fixed rat heart. Details of the MRI sequence are listed in Table 1. Images were phased and the signals from all voxels were averaged and fitted sinusoidally to determine the length of the 360° pulse. Based on the 360° flip angle duration, additional qualitative maps of B₁ homogeneity were acquired on the saline phantom.

SNR Measurements

SNR maps were obtained on both the saline phantom and the fixed rat heart using a gradient-echo pulse sequence. Experimental parameters are listed in Table 1. Images were acquired in 13 contiguous axial slices, followed by acquisition of a noise dataset.

Water and metabolite spectra from a (4 mm)³ voxel, located at the center of the metabolite phantom were obtained using a PRESS sequence (Table 1). Shimming and RF calibration were performed over a (5 mm)³ voxel, centered at the same location. SNR was assessed in all spectra by quantifying the peak area [using a purpose-written time-domain-frequency-domain approach (30)] and dividing it by the standard deviation of the noise (obtained from the last 500 points of the time domain signal). Our software also calculated the Cramer–Rao lower bounds for all fitted parameters. The SNR of the water signals was additionally assessed in the frequency domain using the MR-system software (VnmrJ4, Agilent Technologies, Santa Clara, CA).

Accuracy and Precision of DTI Measurements

To quantify the performance of the new RF-coil design for cardiac DTI measurements, accuracy and precision were evaluated on the fixed rat heart using a bootstrap approach. For this purpose, two-dimensional DTI measurements were repeated five times with each coil, applying the parameters listed in Table 1. For each coil, repetitions were averaged to obtain a reference dataset. Diffusion tensors were calculated on a voxel-by-voxel basis via a weighted linear least-squares fitting method, using in-house software developed in IDL (Exelis, McLean, VA). Tensors were then diagonalized to obtain the sorted eigenvectors ($v_{1,0}$, $v_{2,0}$, $v_{3,0}$) and eigenvalues ($\lambda_{1,0}$, $\lambda_{2,0}$, $\lambda_{3,0}$). From these, reference fractional anisotropy (FA_0) and apparent diffusion coefficients (ADC_0) were calculated using standard methods described elsewhere (31).

A bootstrap method was then applied to generate 100 DTI datasets (32). The eigenvectors and diffusion parameters (FA_i and ADC_i) were computed for each of the resampled datasets. The accuracy of the measurements of FA, ADC, and the primary eigenvector (PEV) v_1 was assessed by comparison with the reference dataset on a voxel-by-voxel basis, whereas precision was estimated by the variability within the resampled datasets. For each voxel n , the accuracy of FA and ADC was assessed using the mean absolute error normalized to the reference values:

$$A_{FA} = \frac{1}{100} \sum_{i=1}^{100} \frac{|FA_i(n) - FA_0(n)|}{FA_0(n)} \quad [1]$$

$$A_{ADC} = \frac{1}{100} \sum_{i=1}^{100} \frac{|ADC_i(n) - ADC_0(n)|}{ADC_0(n)} \quad [2]$$

Deviations in v_1 were determined by measuring the angle θ between the PEV of a given dataset $v_{1,i}(n)$ and the PEV in the same voxel of the reference dataset $v_{1,0}(n)$:

$$\theta_i(n) = \arccos(v_{1,i}(n) \cdot v_{1,0}(n)) \quad [3]$$

To quantify the precision of FA and ADC, the coefficient of variation was calculated. The 95% cone of uncertainty (COU) was measured to assess precision of the PEV orientation (33).

Imaging of a Living Perfused Rat Heart

One heart was excised from a female Sprague-Dawley rat as described in (18). It was connected to the modified perfusion setup and images were acquired along its short axis using a spin echo sequence (Table 1). They were compared to images from the previous studies acquired in similar conditions (18). SNR was evaluated in both dataset by measuring the signal on a voxel-by-voxel basis as the median value over a 3×3 kernel. The noise level was assessed in each slice by computing the standard deviation in a region of interest manually drawn in the background. All animal work was conducted in accordance with the UK Home Office Guidance on the Operation of Animals (Scientific Procedures) Act of 1986, and was approved by Oxford University's ethical review board.

RESULTS

Setup Validation

Bench Measurements

The ratio of the typical volume of interest, based on an isolated heart of an adult rat, and the resonator volume was 25% for the internal and 4.7% for the external birdcage. On the saline phantom, Q factors dropped from unloaded to loaded from 130 to 105 (determined without the final coupling network), resulting in a ratio of 1.24 for the internal resonator (compare external: 250–220, ratio 1.14). S_{11} for the internal birdcage was -23 and -16 dB with loading, showing a channel isolation of 25 dB. The tune S_{11} of the external coil was better than -40 dB and the two channels were isolated by 40 dB.

MR Measurements

The 360° flip angle duration, measured on the saline phantom, was 617.6 ± 2.4 μ s for the internal resonator and 980 ± 13 μ s for the external resonator. This corresponds to a B_1 efficiency of 32.0 μ T $W^{-\frac{1}{2}}$ for the internal resonator, compared to 20.2 μ T $W^{-\frac{1}{2}}$ for the external. On the fixed heart, the 360° flip angle duration was 553.0 ± 4.0 μ s (internal resonator) and 916 ± 14 μ s (external resonator), corresponding to a B_1 efficiency of 35.8 and 21.6 μ T $W^{-\frac{1}{2}}$, respectively. B_1 maps obtained on the saline phantom are shown in the top row of Figure 2.

The mean SNR obtained on the saline phantom with the internal resonator was 64 ± 1 , and 42 ± 1 for the external resonator, representing a gain of 52% (Fig. 2b). The mean SNR obtained on the fixed heart with the internal resonator was 54 ± 4 , whereas it was 34 ± 2 for the external resonator (gain: 59%). Example SNR maps obtained on the fixed rat heart are shown in Figure 2c,c'.

Images obtained with either setup in the midventricular short axis slice of live, Langendorff-perfused rat

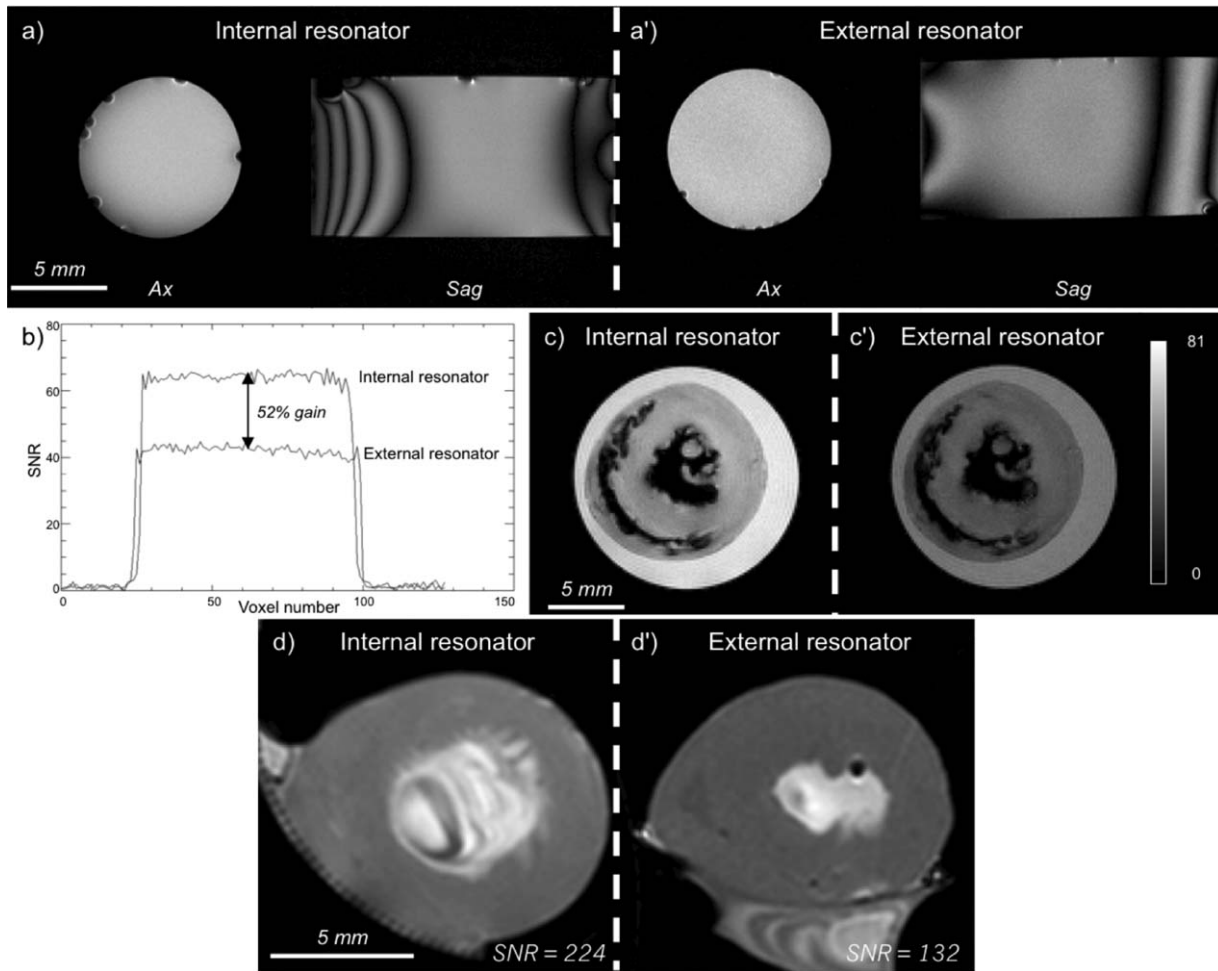


FIG. 2. Coil characterization: Top row: B_1 maps obtained on the homogeneous phantom, in axial (Ax) and sagittal (Sag) orientations using (a) the internal and (a') the external resonator. 10% change in B_1 is observed between two white bands. Middle row: SNR measurements. b: Profiles of SNR across the homogeneous saline phantom; and example of SNR maps obtained on the fixed heart using (c) the internal and (c') the external resonator. Bottom row: Example images obtained on live perfused rat hearts using (d) the internal and (d') the external resonator.

hearts are shown in Figure 2d,d', yielding an SNR of 224 (internal resonator) and 132 (external resonator) (gain: 70%).

The metabolite spectra, shown in Figure 3, illustrate qualitatively the improved sensitivity provided by the internal resonator. Both spectra were 2-fold zero-filled and exponentially filtered (line-broadening: 3 Hz) prior to Fourier transform, and scaled to yield the same noise levels. Quantitative SNR measurements demonstrated an improvement of 1.41 ± 0.42 (fit) and 1.46 ± 0.07 (VnmrJ4), compared to the external resonator. The accuracy of the amplitude estimation in the fitting, as expressed by the Cramer–Rao lower bounds, was 3–5 times better for the internal resonator.

Maps obtained from the bootstrap analysis of the accuracy and precision of DTI measurements are shown in Figure 4 for both resonators. The internal resonator consistently provided better results: the accuracy of the measurements was improved as shown by reductions in the errors in ADC, from 3.4 to 2.4% (reduction: 29%), in FA, from 22 to 18% (reduction: 18%), and in PEV, from 46° to 37° (reduction: 20%). Similarly the uncertainty of

ADC was decreased (and thus the precision improved) from 4.0 to 2.9% (reduction: 28%), the FA from 21 to 18% (reduction: 14%), and the cone of uncertainty from 40° to 32° (reduction: 20%).

DISCUSSION

The aim of the study was to develop and test a novel RF-coil design, optimized for the investigation of live, isolated Langendorff-perfused hearts in a horizontal magnet, and to provide a comprehensive characterization of its utility. It is well-known that RF-coils, optimized for given sample sizes and properties, provide superior SNR performance. Thus, integrating the RF-coil inside the perfusion chamber around the heart is a conceptually obvious approach to meet this aim.

The choice of the birdcage design was primarily based on the ability to operate it in quadrature mode: it is the ideal volume coil for generating uniform circular polarization resulting in an up to $\approx 40\%$ increase in SNR compared to linear polarization from the same coil. At least, 12 legs are required for adequate B_1 homogeneity

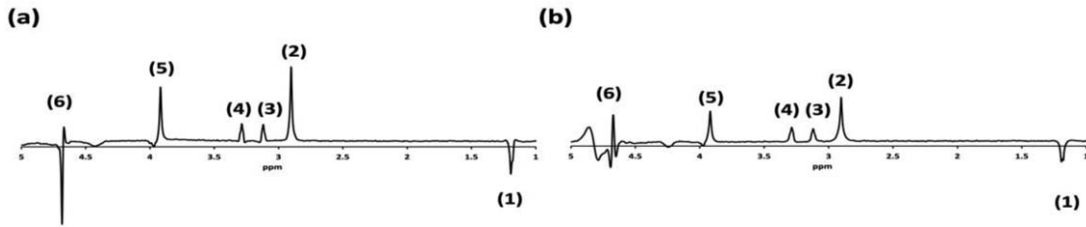


FIG. 3. Metabolite spectra obtained from a $(4\text{ mm})^3$ volume inside the metabolite phantom with (a) the internal and (b) the external resonator to illustrate qualitatively the improved sensitivity provided by the new setup. Both spectra were 2-fold zero-filled and exponentially filtered (line-broadening: 3 Hz) prior to Fourier transform, and scaled to yield the same noise levels. The resonance assignment is: (1) lactate; (2) creatine (CH_3); (3,4) taurine; (5) creatine (CH_2); (6) residual water.

in a closely shielded small birdcage when a relatively large region of uniformity is needed (34). More legs would require a more complex design with potentially a loss in efficiency. Conversely, a solenoid design cannot be operated in quadrature mode, would require a perpendicular design, and thus potentially lead to additional space constraints and hampered workflow. Alternatively, an Rx surface array could be placed inside the perfusion chamber, whereas a Tx volume coil remains outside the sample tube. This would result in an improved filling factor, and may provide additional scan time reduction from the application of parallel imaging. However, small array elements are prone to coil-noise domination, which adversely affects coil array and SNR performance, particularly in center of the array (35).

The new setup yields excellent reproducibility of S_{11} for different loading conditions, at levels that are fully acceptable with respect to reflection of Tx power (less than 3%) and SNR performance. Good channel isolation ensures that the full gain from the quadrature polarization

is obtained during both Tx and Rx. These findings justify the fixed tune-and-match approach of the setup. In addition, the pronounced increase in filling factor results in improved Tx efficiencies and Rx sensitivities. As the saline phantom setup is coil noise dominated (sample resistance less than 25% of coil resistance), one would expect to find Tx efficiency or Rx sensitivity improved by a factor of $\sqrt{(25/4.7)} \approx 2.2$ (gain: 120%), if only considering the increase of the filling factor. In reality, the SNR gain is about 50–70% for all samples. The lower increase could be a result of the generally lower available unloaded Q of the RF-coils with small geometric dimensions. This is also supported by the measured low change in the Q ratio from 1.14 (external) to 1.24 (internal). However, this small change in Q drop would predict a change in Tx efficiency and Rx sensitivity by 27% only, although this is a very rough approximation ($\text{SNR} \sim \sqrt{(1 - Q_{\text{loaded}}/Q_{\text{unloaded}})}$) and neglects various sample loss mechanisms. The effectively observed gain in Tx efficiency and Rx sensitivity (50–70%) lies well between these two approximations.

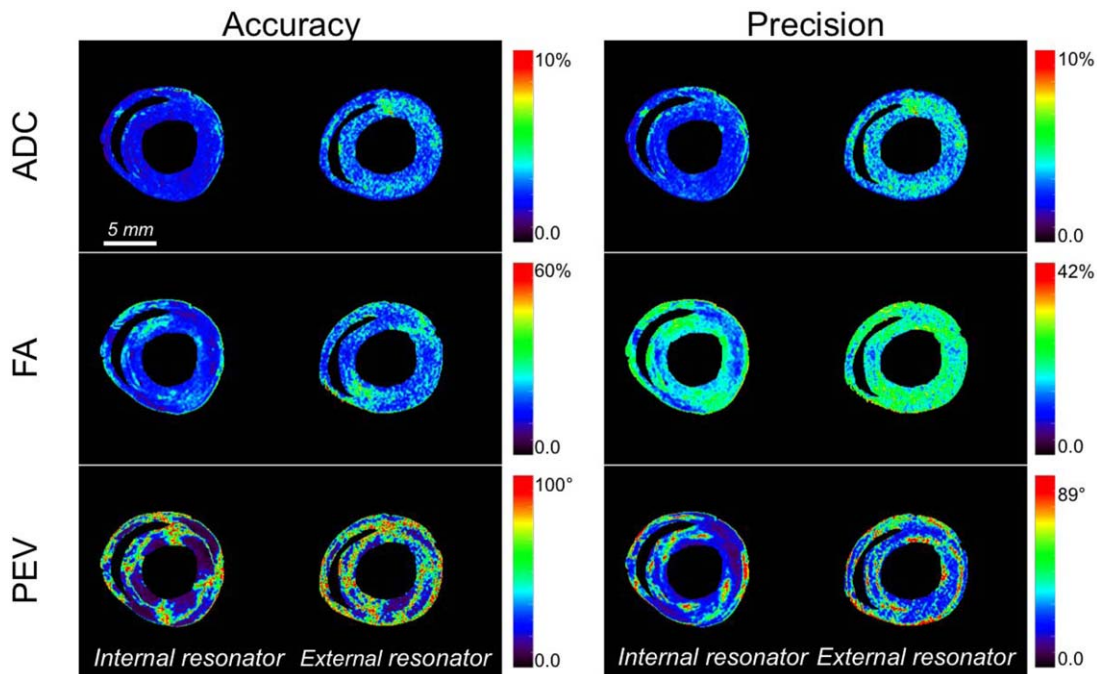


FIG. 4. Improvement in accuracy and precision of DTI measurements (ADC and FA) and locally prevailing cell orientation (fiber orientation) from the orientation of the PEV as assessed by a bootstrap approach on a fixed rat heart.

Phantoms and fixed hearts were used to allow direct side-by-side comparison of the internal and the external resonator. Importantly, an SNR-increase was also observed on the living, Langendorff-perfused rat hearts by retrospectively comparing observations from a previous study (18) to experiments with the new internal resonator. This slightly higher gain (compared to the fixed hearts) is due to the perfusate that reduces the Tx and Rx performance more on the large external resonator than on the smaller internal resonator, i.e., the external resonator “experiences” more losses and increased sample noise from the perfusate than the internal one.

The gain in SNR benefitted DTI and MRS parameters. We found 3–5-fold lower Cramer–Rao bounds for the amplitude estimates (MRS) with the internal resonator. More specifically, creatine for example, which is a major player in the energy metabolism of the myocardium, yielded standard deviations of 0.5% (Cr-CH₃) and 0.7% (Cr-CH₂), respectively. We would therefore expect that fully relaxed spectra on the perfused hearts could be obtained with similar experimental settings within 1 min, which would allow for accurate amplitude estimation (i.e., a standard deviation <10%). We further observed a substantial improvement in the accuracy and precision of DTI measurements, measured by a bootstrap approach (36) on one and same fixed rat heart. Our findings are in agreement with results from previous studies on brain, using simulations (37,38) or in vivo data, where improved SNR was obtained by increasing the number of averages (39,40), the field strength (41,42), or using dedicated RF-coil (27). The influence of SNR on precision and accuracy of muscle DTI was also previously assessed on simulated data (43). For a 2-fold SNR improvement, they demonstrated a gain of 80% in the accuracy of both FA and ADC, and of 50 and 40% in the corresponding precision, respectively. Similarly uncertainty in the PEV orientation was found to decrease with improved SNR in a monotonic fashion. However, these results were obtained by modeling the noise as Gaussian, and using voxels containing only a single fiber orientation. More recently, Hales et al. assessed how both accuracy and precision of the PEV orientation in high-resolution three-dimensional ex vivo cardiac DTI is affected by SNR for various diffusion schemes (44). For the diffusion scheme used in the present study, they reported that the precision of PEV orientation is proportional to $|\text{SNR}|^{-0.71}$ and the accuracy to $|\text{SNR}|^{-0.80}$. The improvement observed with the proposed bootstrap approach in the present study was lower, compared to previous studies. This may be due to the choice of the pulse sequence (two- vs. three-dimensional).

The gain in SNR, obtained through use of optimized hardware, can be utilized in various ways, including (i) reducing scan time by decreasing the number of averages; (ii) increasing spatial resolution; or (iii) improving accuracy of MRS signal amplitude estimation/measured DTI parameters, as demonstrated here. The resulting gain in accuracy can be utilized to reduce the number of animals required to reach statistical significance for any study investigating cardiac structure or metabolism. It is important to highlight that this optimized design will

also benefit any other SNR-constrained and motion-sensitive MR techniques.

In conclusion, we present a novel, optimized RF-coil design for MR investigations of isolated living rat hearts. We report associated MRI improvements and characterized the benefits for DTI and ¹H MRS experiments. This setup may be used to obtain new insight into histo-anatomical properties of the heart, benefit metabolic investigations of the myocardium, and facilitate the further development and application of SNR-constrained and/or motion-sensitive MR techniques.

ACKNOWLEDGMENTS

J.E.S. and P.K. are BHF Senior Basic Science Research Fellows. V.G. and P.K. are supported by a BHF New Horizon Grant. The authors acknowledge Prof. Andrew Blamire's (Newcastle, UK) contribution to the development of the MRS fitting software.

REFERENCES

- Langendorff O. Untersuchungen am überlebenden Säugetierherzen. *Pflügers Archiv für die gesamte Physiologie des Menschen und der Tiere* 1897;66:355–400.
- French BA. Animal models in cardiovascular MRI research: value and limitations. *Curr Cardiovasc Imaging Rep* 2012;5:99–108.
- Ugurbil K, Petelin M, Maidan R, Michurski S, Cohn JN, From AH. High resolution proton NMR studies of perfused rat hearts. *FEBS Lett* 1984;167:73–78.
- Schneider J, Fekete E, Weisser A, Neubauer S, Von Kienlin M. Reduced ¹H-NMR visibility of creatine in isolated rat hearts. *Magn Reson Med* 2000;43:497–502.
- Jacobus WE, Taylor GJ IV, Hollis DP, Nunnally RL. Phosphorus nuclear magnetic resonance of perfused working rat hearts. *Nature* 1977;265:756–758.
- Spindler M, Niebler R, Remkes H, Horn M, Lanz T, Neubauer S. Mitochondrial creatine kinase is critically necessary for normal myocardial high-energy phosphate metabolism. *Am J Physiol Heart Circ Physiol* 2002;283:H680–H687.
- Malloy CR, Buster DC, Castro MMCA, Geraldine CFGC, Jeffrey FMH, Sherry AD. Influence of global ischemia on intracellular sodium in the perfused rat heart. *Magn Reson Med* 1990;15:33–44.
- Bailey IA, Gadian DG, Matthews PM, Radda GK, Seeley PJ. Studies of metabolism in the isolated, perfused rat heart using ¹³C NMR. *FEBS Lett* 1981;123:315–318.
- Allis JL, Snaith CD, Seymour AL, Radda GK. ⁸⁷Rb NMR studies of the perfused rat heart. *FEBS Lett* 1989;242:215–217.
- Fieno DS, Kim RJ, Rehwald WG, Judd RM. Physiological basis for potassium (³⁹K) magnetic resonance imaging of the heart. *Circ Res* 1999;84:913–920.
- Atkinson DJ, Burstein D, Edelman RR. First-pass cardiac perfusion: evaluation with ultrafast MR imaging. *Radiology* 1990;174:757–762.
- Burstein D. MR imaging of coronary artery flow in isolated and in vivo hearts. *J Magn Reson Imaging* 1991;1:337–346.
- Williams DS, Grandis DJ, Zhang W, Koretsky AP. Magnetic resonance imaging of perfusion in the isolated rat heart using spin inversion of arterial water. *Magn Reson Med* 1993;30:361–365.
- Garrido L, Wedeen VJ, Kwong KK, Spencer UM, Kantor HL. Anisotropy of water diffusion in the myocardium of the rat. *Circ Res* 1994;74:789–793.
- Kohler S, Hiller K, Waller C, Bauer WR, Haase A, Jakob PM. Investigation of the microstructure of the isolated rat heart: a comparison between T_2^* - and diffusion-weighted MRI. *Magn Reson Med* 2003;50:1144–1150.
- Chen J, Liu W, Zhang H, Lacy L, Yang X, Song S, Wickline SA, Yu X. Regional ventricular wall thickening reflects changes in cardiac fiber and sheet structure during contraction: quantification with diffusion tensor MRI. *Am J Physiol Heart Circ Physiol* 2005;289:H1898–H1907.

17. Hsu EW, Buckley DL, Bui JD, Blackband SJ, Forder JR. Two-component diffusion tensor MRI of isolated perfused hearts. *Magn Reson Med* 2001;45:1039–1045.
18. Hales PW, Schneider JE, Burton RAB, Wright BJ, Bollensdorff C, Kohl P. Histo-anatomical structure of the living isolated rat heart in two contraction states assessed by diffusion tensor MRI. *Prog Biophys Mol Biol* 2012;110:319–330.
19. Nielles-Vallespin S, Mekkaoui C, et al. In vivo diffusion tensor MRI of the human heart: reproducibility of breath-hold and navigator-based approaches. *Magn Reson Med* 2013;70:454–465.
20. Lau AZ, Tunnicliffe EM, Frost R, Koopmans PJ, Tyler DJ, Robson MD. Accelerated human cardiac diffusion tensor imaging using simultaneous multislice imaging. *Magn Reson Med* 2014. doi: 10.1002/mrm.25200.
21. Gamper U, Boesiger P, Kozierke S. Diffusion imaging of the in vivo heart using spin echoes—considerations on bulk motion sensitivity. *Magn Reson Med* 2007;57:331–337.
22. Nguyen C, Fan Z, Sharif B, He Y, Dharmakumar R, Berman DS, Li D. In vivo three-dimensional high resolution cardiac diffusion-weighted MRI: a motion compensated diffusion-prepared balanced steady-state free precession approach. *Magn Reson Med* 2013. doi: 10.1002/mrm.25038.
23. Sosnovik DE, Mekkaoui C, Huang S, et al. Microstructural impact of ischemia and bone marrow-derived cell therapy revealed with diffusion tensor magnetic resonance imaging tractography of the heart in vivo. *Circulation* 2014;129:1731–1741.
24. Wu M, Tseng WI, Su MM, Liu C, Chiou K, Wedeen VJ, Reese TG, Yang C. Diffusion tensor magnetic resonance imaging mapping the fiber architecture remodeling in human myocardium after infarction: correlation with viability and wall motion. *Circulation* 2006;114:1036–1045.
25. McGill L, Ismail TF, Nielles-Vallespin S, et al. Reproducibility of in-vivo diffusion tensor cardiovascular magnetic resonance in hypertrophic cardiomyopathy. *J Cardiovasc Magn Reson* 2012;14:86.
26. Tunnicliffe EM, Scott AD, Ferreira P, Ariga R, McGill L, Nielles-Vallespin S, Neubauer S, Pennell DJ, Robson MD, Firmin DN. Inter-centre reproducibility of cardiac apparent diffusion coefficient and fractional anisotropy in healthy volunteers. *J Cardiovasc Magn Reson* 2014;16:31.
27. Giannelli M, Belmonte G, Toschi N, Pesaresi I, Ghedin P, Claudio Traino A, Bartolozzi C, Cosottini M. Technical note: DTI measurements of fractional anisotropy and mean diffusivity at 1.5 T: comparison of two radiofrequency head coils with different functional designs and sensitivities. *Med Phys* 2011;38:3205–3211.
28. Hayes CE, Edelstein WA, Schenck JF, Mueller OM, Eash M. An efficient, highly homogeneous radiofrequency coil for whole-body NMR imaging at 1.5 T. *J Magn Reson* (1969) 1985;63:622–628.
29. Hales PW, Burton RA, Bollensdorff C, Mason F, Bishop M, Gavaghan D, Kohl P, Schneider JE. Progressive changes in T_1 , T_2 and left-ventricular histo-architecture in the fixed and embedded rat heart. *NMR Biomed* 2011;24:836–843.
30. Slotboom J, Boesch C, Kreis R. Versatile frequency domain fitting using time domain models and prior knowledge. *Magn Reson Med* 1998;39:899–911.
31. Basser PJ, Mattiello J, Leblhan D. Estimation of the effective self-diffusion tensor from the NMR spin echo. *J Magn Reson Ser B* 1994; 103:247–254.
32. Pajevic S, Basser PJ. Parametric and non-parametric statistical analysis of DT-MRI data. *J Magn Reson* 2003;161:1–14.
33. Jones DK. Determining and visualizing uncertainty in estimates of fiber orientation from diffusion tensor MRI. *Magn Reson Med* 2003; 49:7–12.
34. Doty FD, Entzminger G, Kulkarni J, Pamarthy K, Staab JP. Radio frequency coil technology for small-animal MRI. *NMR Biomed* 2007;20: 304–325.
35. Lanz T, Müller M, Barnes H, Neubauer S, Schneider JE. A high-throughput eight-channel probe head for murine MRI at 9.4 T. *Magn Reson Med* 2010;64:80–87.
36. O’Gorman RL, Jones DK. Just how much data need to be collected for reliable bootstrap DT-MRI? *Magn Reson Med* 2006;56:884–890.
37. Bastin ME, Armitage PA, Marshall I. A theoretical study of the effect of experimental noise on the measurement of anisotropy in diffusion imaging. *Magn Reson Imaging* 1998;16:773–785.
38. Anderson AW. Theoretical analysis of the effects of noise on diffusion tensor imaging. *Magn Reson Med* 2001;46:1174–1188.
39. Farrell JAD, Landman BA, Jones CK, Smith SA, Prince JL, Van Zijl PCM, Mori S. Effects of signal-to-noise ratio on the accuracy and reproducibility of diffusion tensor imaging-derived fractional anisotropy, mean diffusivity, and principal eigenvector measurements at 1.5 T. *J Magn Reson Imaging* 2007;26:756–767.
40. Jeong H, Anderson AW. Characterizing fiber directional uncertainty in diffusion tensor MRI. *Magn Reson Med* 2008;60:1408–1421.
41. Polders DL, Leemans A, Hendrikse J, Donahue MJ, Luijten PR, Hoogduin JM. Signal to noise ratio and uncertainty in diffusion tensor imaging at 1.5, 3.0, and 7.0 Tesla. *J Magn Reson Imaging* 2011;33: 1456–1463.
42. Choi S, Cunningham DT, Aguila F, Corrigan JD, Bogner J, Mysiw WJ, Knopp MV, Schmalbrock P. DTI at 7 and 3 T: systematic comparison of SNR and its influence on quantitative metrics. *Magn Reson Imaging* 2011;29:739–751.
43. Damon BM. Effects of image noise in muscle diffusion tensor (DT)-MRI assessed using numerical simulations. *Magn Reson Med* 2008; 60:934–944.
44. Hales PW, Burton R, Bollensdorff C, Schneider JE. Optimizing accuracy and precision in high resolution diffusion tensor imaging of the ex vivo rat heart. In *Proceedings of the 18th Annual Meeting of ISMRM, Stockholm, Sweden, 2010*. p. 1521.